Author/s:
Robinson, DL;Tse, KM;Franklyn, M;Zhang, JY;Ackland, D;Lee, PVS

Title:
Cortical and Trabecular Bone Fracture Characterisation in the Vertebral Body Using Acoustic Emission

Date:
2019-12-01

Citation:
Robinson, D. L., Tse, K. M., Franklyn, M., Zhang, J. Y., Ackland, D. & Lee, P. V. S. (2019). Cortical and Trabecular Bone Fracture Characterisation in the Vertebral Body Using Acoustic Emission. Annals of Biomedical Engineering, 47 (12), pp.2384-2401. https://doi.org/10.1007/s10439-019-02316-y.

CORTICAL AND TRABECULAR BONE FRACTURE CHARACTERISATION IN THE VERTEBRAL BODY USING ACOUSTIC EMISSION

Dale L. Robinson[a] , Kwong Ming Tse[a], Melanie Franklyn[b], Jiang Yue Zhang[c], David Ackland[a], Peter Vee Sin Lee[a]

[a]Department of Biomedical Engineering, University of Melbourne, Melbourne, Victoria, Australia

[b]Defence Science and Technology Group, Melbourne, Victoria, Australia

[c]The Johns Hopkins University Applied Physics Lab, Laurel, Maryland, United States

Submitted as an original article to the journal Annals of Biomedical Engineering

Word count: Text: 6,057 (Introduction to Discussion), Abstract: 199.

14 May 2019

Corresponding author:

Peter Vee Sin Lee
Department of Biomedical Engineering
University of Melbourne, Victoria 3010, Australia
Email: pvlee@unimelb.edu.au
Phone: +61 3 8344 4426
Fax: +61 3 8344 4290

Abstract:

The ability to rapidly detect localised fractures of cortical and/or trabecular bone sustained by the vertebral body would enhance the analysis of vertebral fracture initiation and propagation during dynamic loading. In this study, high rate axial compression tests were performed on twenty sets of three-vertebra lumbar spine specimens. Acoustic Emission (AE) sensor measurements of sound wave pressure were used to classify isolated trabecular fractures and severe compressive fractures of vertebral body cortical and trabecular bone. Fracture detection using standard AE parameters was compared to that of traditional mechanical parameters obtained from load cell and displacement readings. Results indicated that the AE parameters achieved slightly enhanced classification of isolated trabecular fractures, whereas the mechanical parameters better identified combined fractures of cortical and trabecular bone. These findings demonstrate that AE may be used to promptly and accurately identify localised fractures of trabecular bone, whereas more extensive fractures of the vertebral body are best identified by load cell readings due to the considerable loss in compressive resistance. The discrimination thresholds corresponding to the AE parameters were based on calibrated measurements of AE wave pressure and may ultimately be used to examine the onset and progression of vertebral fracture in other loading scenarios.

Key terms: Acoustic emission, dynamic compression, lumbar spine vertebrae, vertebral fracture

1 Introduction

Vertebral fractures are a frequent and debilitating injury primarily associated with osteoporosis in the elderly,[4] traumatic events such as falls and vehicular accidents,[29] or underbelly blast attacks on military vehicles.[37] Post-injury outcomes remain poor, as evidenced by high rates of morbidity associated with neurological deficit, chronic back pain and functional impairment.[13,16] Prevention of vertebral fracture remains challenging, since the mechanisms governing the initiation and propagation of fracture are not well understood.[7] For compression-induced fractures sustained by the vertebral body, such as crush, burst, or biconcave fractures, cadaveric models have shown that localised damage to the vertebral endplate and underlying trabecular bone comprise the principal feature of vertebral fracture initiation.[18,20] However, detection of isolated trabecular bone injuries, including micro-damage or micro-fracture, remains challenging since localised bone behaviour is difficult to quantify in real time. As a result, studies of injury due to high-rate loading have largely been limited to post-test medical imaging.[3,32,36] A reliable technique that allows the rapid identification and differentiation between different vertebral fracture types is not yet available.

Measurement of change in stiffness of a spine specimen under compressive loading has been used to identify bone fracture during testing[9,33]; however, isolated fractures of trabecular bone may not considerably alter the total vertebral stiffness and therefore, may go undetected.[5] High-resolution medical imaging such as micro-computed tomography (μCT) can be used to identify micro-fractures after loading, but the vast amount of image data can be time consuming to analyse. While μCT has been used to visualise bone fracture using incremental quasi-static loading,[18,24] three-dimensional imaging sequences are not yet capable of acquiring the temporal characteristics of a bone fracture, as fracture initiation

and propagation has been observed to occur in less than 0.50 ms.[19]

An alternative approach to detecting a fracture event is with Acoustic Emission (AE) sensors, which detect the transient elastic waves generated by the localised releases of strain energy. This approach has been used to identify severe compression fractures of the vertebral body under dynamic axial compression[11,36] and has demonstrated thresholds in AE amplitude, timing and frequency content that corresponded to the fracture event. However, these studies reported axial strains in excess of 25% of the vertebral body height and did not distinguish between cortical and trabecular bone failure. In a further study of two vertebrae specimens, AE count was observed to be different between normal and osteopenic bone.[15] AE signal characteristics have also been evaluated during fracture of femora,[2] as well as for isolated samples of trabecular[38] and cortical bone,[1] involving a range of different loading conditions. To our knowledge, no previous studies have used AE signals for the identification of fractures localised to the trabecular bone during compression of vertebrae.

The aims of this study were twofold: firstly, to obtain AE signals corresponding to isolated trabecular bone fractures and compression fractures involving both trabecular and cortical bone of lumbar vertebrae tested in dynamic axial compression, and secondly, to compute the classification characteristics for these different fracture types based on AE signal parameters and presence of yielding, maximum load, and decrease in fracture load. The AE voltage was calibrated to provide measurements of acoustic wave pressure,[12] which has not been previously used for AE analysis of bone fracture. Since thresholds related to different AE parameters have been previously identified for severe bone fractures,[8,36] and for discriminating between failure modes in composite materials,[23] it was hypothesised that AE thresholds may be used to identify and differentiate between fractures of trabecular and cortical bone.

2 Materials and Methods

2.1 Specimen preparation

Spinal segments extending from T12 to S1 were sourced from fifteen male cadavers (age: 61.5 ± 9.8 years, weight: 80.0 ± 26.0 kg, height: 176.5 ± 10.0 cm) that had no history of spinal surgery and were free of macroscopic abnormalities, including bridging osteophytes, or wedge deformities. The spinal segments were separated into twenty three-vertebra specimens comprising three adjacent vertebrae taken at any of the five positions between T12 and S1 (Table 1), two intervertebral discs, and the major spinal ligaments (anterior longitudinal ligament, posterior longitudinal ligament, ligamentum flavum, intertransverse ligament, interspinous ligament and supraspinous ligament, facet capsulary ligaments). The facet joints and associated capsulary ligaments were left intact, and all other soft tissue removed. Specimens were kept hydrated by regular irrigation with 0.9% saline at all times during this study. Ethics approval for this study was obtained from the University of Melbourne Human Ethics Committee (ID: 1647558).

2.2 Imaging and processing

Each three-vertebra specimen was imaged prior to mechanical testing using a small animal computed-tomography (CT) scanner (Inveon; Siemens, Munich, Germany), where the axial slice thickness and in-plane resolution were each 0.1 mm. To identify bone fractures, this scan was repeated for the centre vertebrae after mechanical testing. A water-filled bone mineral density (BMD) phantom with densities of 0, 250, 500, 750 and 1000 g/cm^3 (Computerized Imaging Reference Systems, Norfolk, VA) was included in each scan. A linear regression was fitted to the greyscale values of these five known densities, which allowed the CT voxels to be converted to apparent bone mineral density (ρ_{app}). The ρ_{app} was then

converted to Young's modulus, *E*, based on the power law for vertebral trabecular bone[26] (Eq. 1).

$$\boldsymbol{E = 4730\rho_{app}^{1.56}} \quad (1)$$

where *E* is in MPa and ρ_{app} is in g/cm^3.

The specimen height was quantified by the anterior height of the centre vertebral body and lower intervertebral disc (h_{VB+IVD}) and the mid-body height of the centre vertebral body and intervertebral discs (h_{mid}) (Fig. 1a). The voxels in the axial mid-plane of the centre vertebral body (Fig. 1b) were used to derive the axial rigidity (EA) and cross-sectional area (a_{VB}) (Eqs. 2 and 3, respectively). The presence of Schmorls nodes or disc herniation into the endplate were identified using the CT images, and the more severely degraded disc for each specimen was graded according to clinical radiographic criteria.[21] The volumetric BMD (vBMD) of trabecular bone was determined for the centre vertebral body using previously published methods.[43]

$$\boldsymbol{EA = \sum_i E_i a_i} \quad (2)$$

$$\boldsymbol{a_{VB} = \sum_i a_i} \quad (3)$$

where the subscript i denotes the voxel number.

2.3 Instrumentation and mechanical testing

Two miniature Acoustic Emission (AE) sensors (S9225; Physical Acoustics Corp., Mistras Group, Princeton Junction, USA) with a peak sensitivity of -85 dB, ref 1V/µPa and a stable operating frequency of approximately 100-1000 kHz were attached to the body of the centre vertebra by a process of smoothing the bony surface with a scalpel and sandpaper, degreasing with ethanol, filling the pores and waterproofing the surface with polyurethane, and bonding the sensor with cyanoacrylate glue.[35] One AE sensor was placed on each of the

left and right lateral surfaces of the centre vertebra of each cadaveric specimen (Fig. 2). Each sensor used a pre-amplifier with a bandpass filter of 10 kHz to 1200 kHz to remove noise outside of the range expected for bone fracture.[11] The AE signals were recorded using a data acquisition system with a sampling rate of 2 MHz (USB-6366; National Instruments Corp., Austin, USA). The AE signal voltage was converted to AE wave pressure using the manufacturer-supplied sensitivity curve for each sensor, a method which decouples the resonant response of the sensor from the signal (Fig. 3).[17]

To enhance the potting fixation of the spine specimens, metal screws were drilled into the outer vertebral bodies and steel wire was tightly wound between each screw head. Using a customised positioning apparatus, each specimen was oriented with the inferior and superior vertebral rims of the centre vertebra horizontal, whilst the upper and lower vertebrae remained in their unloaded position (Fig. 2). The upper and lower vertebrae were then potted below the intervertebral discs in an aluminium fixture using dental plaster. Care was taken to ensure the facet joints and spinous process of the centre vertebra were not impeded by plaster.

Each potted spine was secured to a calibrated material testing machine (model 8874; Instron, Norwood, USA), with the upper aluminium fixtures attached to the hydraulically-driven piston and the lower aluminium fixtures attached to a six degree-of-freedom load cell (MC5; AMTI, Watertown, USA) mounted on the base of the machine (Fig. 2). The vertical component of the force and piston displacement represented the axial spine compressive force (F_z) and displacement (d_z), respectively. Using adjustable plates, the potted spine was translated in the axial plane so that a 500 N compressive load produced near-uniform axial compression, defined by flexion-extension and lateral bending moments of less than 1 Nm. From an unloaded position, each spinal specimen was tested in a loading sequence that

comprised:

(1) Preloading: 5 cycles at 1 Hz from 0 to 0.1 mm of compression.

(2) Dynamic loading: Compression at maximum acceleration of the testing machine to a specified displacement. Depending on the amount of displacement (1 to 12 mm), these accelerations resulted in peak velocities between 0.1 and 0.9 m/s.

(3) Unloading: Returning the spine to its unloaded position in 1 s.

(4) Recovery: Resting the specimen in an unloaded position for approximately 30 minutes.

The entire loading sequence was repeated in increments of 4% increase in the displacement relative to h_{VB+IVD} until a fracture was detected by a visible crack on the left or right surface of the centre vertebral body, or a negative slope in the force-displacement curve.[36] After testing, each specimen was removed from the testing machine and visually examined for damage to ligaments, discs and cortical bone. The centre vertebra was extracted and imaged by CT to analyse and classify bone fracture. To evaluate if the AE signal was potentially affected by noise from the surrounding potting and testing apparatus, the compression test was repeated with the spinal specimen replaced by a 50 mm diameter aluminium rod with two attached AE sensors (see Supplementary Fig. 1). For five compressions up to 10 kN, the AE wave pressure was less than 130 Pa (see Supplementary Fig. 2), a magnitude which would be reduced by signal attenuation across the spinal specimen and, hence, sufficiently small to suggest noise had a relatively minor effect on the AE measurements.

2.4 Acoustic emission parameters

For the sensor with the largest AE signal magnitude of each test, standard AE parameters were calculated from the AE sound pressure (Fig. 4). The absolute maximum of the AE signal

($AE_{amplitude}$) was identified, and using an AE limit of 10 Pa to eliminate background noise, AE_{counts} was computed as the total number of crossings above this limit. AE bursts representing discrete periods of AE activity were identified as the total interval where consecutive AE signal peaks exceeded the AE limit. AE rise time and duration ($AE_{risetime}$ and $AE_{duration}$, respectively) were calculated from the burst containing the largest $AE_{amplitude}$. The total acoustic emission energy (AE_{energy}) was calculated from the raw AE signal using Eq. (4). To provide a measure of AE energy that was independent of the sensor, the AE sound exposure ($AE_{exposure}$) was calculated (Eq. 5), which was proportional to AE_{energy} and utilised the calibrated AE wave pressure readings. AE parameters were calculated over the first 50 ms from the start of the compression, which captured the dynamic loading interval.

$$\boldsymbol{AE_{energy} = \int_{t_0}^{t_1} V(t)^2 dt} \quad (4)$$

$$\boldsymbol{AE_{exposure} = \int_{t_0}^{t_1} p(t)^2 dt} \quad (5)$$

where AE_{energy} = acoustic emission energy, V=acoustic emission voltage, t=time, t_0=initial time, t_1=final time, $AE_{exposure}$ = acoustic emission sound exposure, p=acoustic emission wave pressure.

2.5 Mechanical parameters

The engineering stress (σ_z) and strain (ε_z) in each cadaveric specimen were calculated (Eqs. 6 and 7), where a_{VB} was assumed to remain constant. Yielding was then identified according to the 0.2% offset rule[9] (Fig. 5). The presence or absence of yielding was quantified by the binary variable Yield State, as 1 and 0, respectively, and the yield stress and corresponding force ($\sigma_{z,Y}$, $F_{z,Y}$, respectively) were extracted at the yield point. The maximum stress and corresponding force ($\sigma_{z,max}$, $F_{z,max}$, respectively) were also obtained for each test. Since ε_z represented deformation of both the vertebral body and the inferior disc, the maximum

strain of the vertebral body ($\varepsilon_{z,max}$), was recalculated (Eq. 8). The change in force and stress following the peak stress (ΔF_z and $\Delta\sigma_z$) were also quantified as a measure of bone fracture damage (Fig. 5).

$$\sigma_z = \frac{F_Z}{a_{VB}} \tag{6}$$

$$\varepsilon_z = \frac{d_Z}{h_{total}} \tag{7}$$

$$\varepsilon_{z,max} = \frac{F_{z,max}}{EA} \tag{8}$$

2.6 Fracture classification

All mechanical tests were classified as one of the following injury categories:

- Category 1: No injury. The first compression test of each specimen (i.e. 4% total strain of three-vertebra specimen) was assumed to be a sufficiently small amount of compression such that no bone fracture was sustained.
- Category 2: Isolated trabecular fracture. The final compression test on a specimen that resulted in a fracture encompassing only trabecular bone.
- Category 3: Combined cortical and trabecular fracture. The final compression test on a specimen that resulted in a fracture that extended through both the cortical shell and trabecular bone.
- Category 4: All remaining tests, where it was unknown if the test had resulted in bone injury. Tests in this category were not considered for further analysis.

Fractures were identified by CT image analysis. The bony geometry of each pre- and post-test centre vertebra were registered using a mutual information metric[25] in Slicer 3D (Slicer 4.6.2; Massachusetts Institute of Technology, Cambridge, USA) and segmented with identical intensity thresholds. Once registered, obvious fractures encompassing both the cortical and trabecular bone were visually identified. Specimens that did not appear to exhibit a

significant fracture were considered for further image analysis using a method similar to that used for bone remodelling analysis[6], where their pre- and post-test image datasets (Fig. 6a and b respectively) were imported into Matlab (version R2016b; Mathworks, Natick, MA), and their difference in intensities calculated (Fig. 6c). Potential fracture sites were taken as regions where the intensity differed by greater than 30% (Fig. 6f), a cut-off which was chosen to provide a reasonable number of sites for further analysis (approximately 20 per specimen). At each site, a 1 mm cube was segmented from the pre- and post-test geometries, from which volumetric meshes were generated to identify regions of fractured bone (Figs. 6d and 6e).

2.7 Statistical analysis

Significant differences in the AE and mechanical parameters between the different categories of fracture status were assessed by a two-sample Kolmogorov-Smirnov test ($p<0.05$) which makes no assumption about the distribution of the data. The ability of explanatory variables to classify the fracture types was assessed using a receiver operating curve (ROC) analysis. The ROC describes the performance of a classification variable to correctly predict a particular outcome as its discrimination threshold is varied. The area under the receiver operating curve (AUC) was evaluated, which describes the overall probability that a variable will correctly classify an outcome. At each point of the ROC, the sensitivity (proportion of cases correctly identified with the outcome), the specificity (proportion of cases correctly identified without the outcome) and accuracy (proportion of all positive and negative outcomes correctly identified) was calculated (Eqs. 9, 10 and 11 respectively). Optimal values for the sensitivity, specificity, accuracy and the discrimination threshold were selected based on the maximum Youden's J statistic, which represents the

maximum correct classification rate. The significance of each AUC was calculated compared to an AUC of 0.5 (i.e., random classification) using the Mann-Whitney (Wilcoxon) test.

$$\boldsymbol{Sensitivity} = \frac{\boldsymbol{TP}}{\boldsymbol{TP+FN}} \tag{9}$$

$$\boldsymbol{Specificity} = \frac{\boldsymbol{TN}}{\boldsymbol{TN+FP}} \tag{10}$$

$$\boldsymbol{Accuracy} = \frac{\boldsymbol{TP+TN}}{\boldsymbol{TP+TN+FP+FN}} \tag{11}$$

where TP is the true positive rate, TN is the true negative rate, FN is the false negative rate and FP is the false positive rate.

The ROC curve was derived using independent analyses with predictors that included the acoustic emission parameters (AE_{energy}, $AE_{exposure}$, $AE_{amplitude}$, $AE_{risetime}$, $AE_{duration}$, AE_{counts}) and the mechanical parameters ($Yield_{state}$, $F_{z,max}$, $\sigma_{z,max}$, $\varepsilon_{z,max,}$ ΔF_z, $\Delta\sigma_z$). The yield force and stress were not considered as predictors because most tests classified as Category 1 had not experienced yielding. The ability of each predictor to distinguish between the different types of fracture status was assessed for the following cases:

(i) Category 1: No fractures from Category 2: Isolated trabecular fractures, and

(ii) Category 1: No fractures from Category 3: Combined cortical and trabecular fractures.

To evaluate how the sensor location influenced the fracture identification, the ROC was calculated for each AE parameter of the AE sensor with the lower $AE_{amplitude}$. The classification accuracy (Eq. 11) was then determined at the ROC position corresponding to the previously identified discrimination threshold of the first AE sensor. All statistical analyses were performed using SPSS (version 24; SPSS Inc., Chicago, IL, USA).

3 Results

All fractures identified in the current study were confined to the vertebral body, and no specimen sustained ligament rupture or damage to the intervertebral disc upon inspection and dissection of the discs after testing. Of the twenty lumbar spine specimens tested in axial compression, the final tests for thirteen specimens were identified to be a combined cortical and trabecular fracture (Category 3). The most prevalent injury types for these specimens were cranial endplate fractures, or split coronal fractures extending caudally from the cranial end plate (Fig. 7a and 7b, respectively). Five specimens sustained an isolated trabecular fracture (Category 2), with fracture locations distributed randomly within the vertebral body, as shown in Fig. 6. For the initial compression tests of 14 specimens, the peak compressive force ($F_{z,max}$) (2.1±0.6 kN) was low compared to reported fracture loads for lumbar vertebrae,[28,34,40] and a visual examination found no indication of a sustained fracture; hence, these tests were classified as Category 1. For four specimens, the initial compression tests were excluded from subsequent analyses due to data acquisition problems. The remaining two specimens did not sustain a fracture and their complete sequence of compression tests were classified as Category 1. In terms of disc degradation, seven specimens were graded as 0 (normal), seven as 1 (mild) and six as 2 (moderate), and 0 with as 3 (severe), however, there was no significant differences in the disc grading between Category 1, 2 and 3 (Table 2), and no specimens were identified to have herniation of the disc into the endplate. Notably, two specimens from Category 2 and six specimens from Category 3 were found to have pre-existing Schmorls nodes, indicating that the condition of the nucleus has some influence on the nature of the sustained fracture.

The only descriptive characteristic to vary significantly between the injury categories

was h_{VB+IVD}, which was smaller for Category 2 than either Category 1 or Category 3 (each $p<0.05$; Table 2), suggesting that shorter specimens were more likely to sustain isolated trabecular fractures. Whilst not significant, it was notable that on average the variables $F_{z,Y}$ and $\sigma_{z,Y}$ of Category 2 were greater than those of Category 3. All AE parameters were significantly different for Category 1 vs Category 2 (each $p<0.05$), and for Category 1 vs Category 3 (each $p<0.001$). This was also the case for all the mechanical parameters, apart from the yield strength variables ($F_{z,Y}$ and $\sigma_{z,Y}$). Since there were many tests where yielding was not observed, $F_{z,Y}$ and $\sigma_{z,Y}$ comprised of only four tests for Category 1 and due to this lower statistical power it did not vary significantly between any of the injury categories. Notably, the mechanical parameters $\Delta F_{z,max}$ and $\Delta\sigma_{z,max}$ were the only variables that were significantly different between the tests for Category 2 and 3 ($p<0.05$).

For classification between Category 1 and 2, the mean AUC with the greatest magnitude was observed for the acoustic emission parameter $AE_{duration}$ (AUC: 0.98, 95% CI: 0.94-1.00, $p<0.001$) (Table 3). Youden's J statistic was greatest for this variable, which indicated the optimal combination of sensitivity and specificity (100% and 95.5%, respectively), with a corresponding threshold of 0.63 ms. The parameters AE_{energy}, $AE_{exposure}$, $AE_{amplitude}$ and $AE_{risetime}$, also had very good classification characteristics, with mean AUCs between 0.95 and 0.97. The thresholds for $AE_{exposure}$ and $AE_{risetime}$ (5713.9 $Pa^2 \cdot s$ and 0.31 ms, respectively) also separated Category 1 from 2 with an ideal sensitivity (each 100%), and a high specificity (86.4% and 90.9%, respectively). The greatest AUC of the mechanical parameters was obtained for $\varepsilon_{z,max}$ (AUC: 0.95, 95% CI: 0.86-1.00, $p<0.001$), whilst the parameters $Yield_{state}$, $F_{z,max}$, $\sigma_{z,max}$ also achieved good classification performance with mean AUCs between 0.90 and 0.93. The thresholds for these parameters separated Category 1 and 2 with a sensitivity of 100%, and specificities that ranged from 77.3% to 81.8%.

When differentiating between Category 1 and 3, the mechanical parameters $\Delta F_{z,max}$ and $\Delta\sigma_{z,max}$ each demonstrated ideal classification (AUC: 1.00, 95% CI: 1.00-1.00, p<0.001) (Table 4). The thresholds for $\Delta F_{z,max}$ and $\Delta\sigma_{z,max}$ were 711.4 N and 0.5 MPa, respectively, each had a sensitivity and specificity of 100%, meaning a drop in force or stress greater than these amounts differentiated all tests with a combined cortical and trabecular fracture from tests without injury. In relation to the AE parameters, the mean AUC was greatest for the variables AE_{energy} (AUC: 0.98, 95% CI: 0.94-1.00, p<0.001), $AE_{exposure}$ (AUC: 0.98, 95% CI: 0.95-1.00, p<0.001), $AE_{amplitude}$ (AUC: 0.98, 95% CI: 0.93-1.00, p<0.001) and $AE_{duration}$ (AUC: 0.98, 95% CI: 0.95-1.00, p<0.001). The thresholds for AE_{energy}, $AE_{exposure}$, $AE_{amplitude}$ and $AE_{duration}$ (2.77e-3 V^2·s, 3945.1 Pa^2·s, 642.7 Pa and 0.66 ms, respectively) had a sensitivity that ranged between 92.3% and 100%, with a corresponding specificity between 84.6% and 95.5%.

The classification accuracy of the AE parameters for the AE sensor with the greater $AE_{amplitude}$ varied from 85.2% to 96.3% for classification between Category 1 and 2 (Table 3) and 90.3% to 94.3% for classification between Category 2 and 3 (Table 4). Based on the discrimination thresholds obtained from this sensor, the classification accuracy derived for the second AE sensor attached to each specimen was similar when classifying Category 1 and 2 (87.3 to 96.3%; Table 3), however, reduced when classifying Category 1 and 3 (79.7% to 89.3%; Table 4).

The distinctive differences in the AE wave pressure, displacement and force traces were apparent when comparing repeated tests on specimen that were ultimately classified as Category 2 and 3 (Fig. 8). For the third test on the specimen designated as Category 2 (Fig. 8c), the peak in the AE wave pressure exceeded the $AE_{amplitude}$ threshold corresponding to an isolated trabecular fracture (461.9 Pa; Table 3). The third test of the specimen designated as Category 3 (Fig. 8f) exceeded the $AE_{amplitude}$ threshold corresponding to a combined cortical

and trabecular (642.7 Pa; Table 4), as well as the threshold for the isolated trabecular fracture. For this more severely fractured specimen, the AE wave pressure exceeded each of these thresholds prior to the identified yield point.

4 Discussion

To address the technical challenge in detection of bony fracture during high-rate mechanical loading, the present study reports an experimental method employing AE signal parameters for the identification of both isolated trabecular fractures in addition to more severe fractures encompassing both cortical and trabecular bone of the vertebral body. The classification performance of the AE parameters was compared to that using standard mechanical parameters derived from compressive force and displacement measurements. Due to the sensitivity of AE sensors in detecting transient vibrations from localised bony fractures, it was found that these sensors would allow a more accurate and rapid identification of different fracture types from biomechanical testing of cadaveric bone specimens, such as lumbar spine vertebrae. To obtain sensor-independent measurements, all AE parameters other than the AE energy were calculated based on the AE wave pressure.

When differentiating between mechanical loadings that resulted in isolated trabecular fractures and tests that did not result in any fracture, the acoustic emission exposure ($AE_{duration}$) provided the best classification (AUC: 0.98, 95% CI: 0.94-1.00, $p<0.001$) (Table 3). The classification performance of the AE parameters, AE_{energy}, $AE_{exposure}$, $AE_{amplitude}$ and $AE_{risetime}$ was also high, each with a mean AUC between 0.95 and 0.97 (each $p<0.001$) (Table 3). Hence, the corresponding thresholds for AE_{energy}, $AE_{exposure}$, $AE_{amplitude}$, $AE_{risetime}$ and $AE_{duration}$ (0.05e-3 V^2·s, 5713.9 Pa^2·s, 461.9 Pa, 0.31 ms and 0.63 ms respectively) may be used for classification of isolated trabecular fractures with ideal sensitivity (detection rate of

tests with fracture) of 100%, and a specificity (detection rate of tests without fracture) ranging between 81.8 and 95.5%. Encouragingly, the classification accuracy based on these thresholds was similar for both AE sensors attached to each vertebral body (85.2% to 96.3%; Table 3). This would suggest that classification of this fracture type based on the AE signal was relatively insensitive to location, provided the AE sensor was directly attached to the vertebral body that incurred the fracture. The ability of the mechanical properties to classify isolated trabecular fractures was slightly reduced compared to the AE properties, with the Yield state, $F_{z,max}$, $\sigma_{z,max}$ and $\varepsilon_{z,max}$ having a mean AUC ranging between 0.90 to 0.95 ($p<0.001$) and their corresponding thresholds had a sensitivity of 100%, together with a specificity between 77.3 and 81.8%.

When classifying fractures that encompassed both cortical and trabecular bone from tests without fracture, the mechanical parameters describing the drop in compressive force and stress after the peak force ($\Delta F_{z,max}$ and $\Delta\sigma_{z,max}$) each provided ideal classification (AUC: 1.00, 95% CI: 1.00-1.00, $p<0.001$) (Table 4). The optimal threshold for $\Delta F_{z,max}$ and $\Delta\sigma_{z,max}$ of 711.4 N and 0.5 MPa, respectively, each had a sensitivity and specificity of 100% meaning these magnitudes differentiated all tests with a cortical and trabecular fracture from tests without an observed fracture. The classification performance of the AE properties AE_{energy}, $AE_{exposure}$, $AE_{amplitude}$ and $AE_{duration}$ was marginally lower than the mechanical properties with a mean AUC of 0.98 each ($p<0.001$). The optimal thresholds for these variables were able to classify the cortical and trabecular fractures with sensitivities between 84.6% and 100% and specificities of 84.6% to 100.0%. However, the classification accuracy for this fracture type varied between the two AE sensors attached to each vertebra (Table 4), suggesting that classification of these fractures based on the AE signal was sensitive to the sensor location.

The vBMD of the 20 lumbar specimens (162.1±53.7 mg/cm^3; Table 1), had a relatively

wide range compared to previous studies,[42,43] which indicates the findings in the current study may be generalisable to a wide range of different lumbar vertebrae. The results indicate that when distinguishing between tests with and without injuries to the vertebral body, AE parameters provide improved classification of isolated trabecular fractures, whilst the mechanical parameters better distinguish the more severe fractures of both cortical and trabecular bone. Despite the methodological differences in these two techniques, the classification performance using either the AE or mechanical parameters was relatively similar, suggesting that either set of parameters may be effective for classification of isolated trabecular or combined cortical and trabecular fracture. However, an advantage of using the AE parameters is that the thresholds identified in the current study may be used to identify the timing of different types of bone fracture. This was demonstrated for two representative specimens, where the AE wave pressure exceeded the threshold for an isolated trabecular fracture (Fig. 8c) and combined cortical and trabecular fracture (Fig. 8f), the latter of which indicated fracture before any apparent yielding of the specimen, a behaviour consistent with previous work.[41] This application still requires further validation of vertebral compression using CT, where the loading is carefully controlled to cause the AE parameters to exceed their respective thresholds, whilst no yielding or fracturing is observed according to the mechanical parameters.

Although it was reasonable to expect an association between the drop in compressive load and vertebral fracture, this study provides measurements of the amount of load drop that would accompany the injury. The drop in compressive load observed for vertebral fracture was consistent with Jackman et al.,[18] who reported a force reduction of 280 ± 220 N at the onset of vertebral fracture for three-vertebrae thoracic specimens tested in axial compression. The magnitude of the force reduction reported by Jackman et al. was

lower than that of the current study, which may be attributed to differences in the specimens (i.e. thoracic vertebral bodies versus intact lumbar vertebrae) and testing method (quasi-static compared to dynamic compression). Nonetheless, these results of the present study suggest that the drop in compressive resistance may be used to identify severe fractures sustained by the vertebral body for dynamic loading.

A hallmark of all fracture types observed in the current study was combined cortical and trabecular fractures encompassed the cranial endplate. This behaviour was likely due to the higher porosity and lower thickness observed for this region than those of the caudal endplate and cortical shell, which may render it more prone to damage.[18,44] Furthermore, the isolated trabecular fractures sustained by the five specimens may be considered a severe form of trabecular micro-fracture experienced by the vertebral body in vivo without inducing an extensive failure of the cortical shell.[39] Nonetheless, one may expect that some degree of trabecular fracturing would precede a cortical fracture and, indeed, the AE signals qualitatively indicated such behaviour may take place, where a small burst in AE signal activity was regularly noted before the large peak likely indicative of cortical fracture (Fig. 8). Although an analysis of the timing of different fracture types and temporal AE energy characteristics was too extensive to incorporate into the current study, the identified AE signal thresholds may be extended in future research by exploring this relationship.

There was an unexpected trend observed in the mechanical parameters for Categories 2 and 3, where the maximum compressive force and stress were on average higher for the isolated trabecular fractures compared to the more severe combined cortical and trabecular fractures (Table 2). Although this difference was not significant, it would likely be explained by differences in the stiffness and size of specimens comprising the different fracture categories, as evidenced by EA, which was on average greater for Category 2 than

Category 3, and the significantly shorter specimen height (h_{VB+IVD}) for Category 2 than Category 3 ($p < 0.05$; Table 2). The lower height of specimens comprising Category 2 may suggest that shorter specimens are more resistant to sustaining cortical fractures, possibly because they are less susceptible to bending or buckling of the cortical shell; however, this hypothesis requires further examination with a larger sample size.

This is the first study in which the classification performance of AE parameters related to bone fracture has been determined. However, the AE signal characteristics for fracture and non-fracture tests of a small group of vertebral bodies under axial compression was analysed in a previous study, where the $AE_{amplitude}$ was greater for injurious tests compared to those without injury,[36] in agreement with the findings of the present study. The uncalibrated sensor voltages from the AE signal for combined cortical and trabecular fractures (1.60±1.43V) were of a similar magnitude to those observed for fractured vertebrae and femora using identical AE sensors,[11,31] which supports the validity of our AE data acquisition system. The AE signal duration for combined cortical and trabecular fractures ($AE_{duration}$) was found to be 6.0±4.1 ms, which tended towards the upper limit of AE burst durations reported for vertebral fractures (0.15-10 ms).[11] The longer AE signal durations in the current study was most likely due to the greater loading rates considered by Goodwin et al.[11] of 2.9 m/s, since acoustic emission signals for vertebral fractures are thought to be sensitive to the rate of load application.[3]

In previous research, a relationship between the frequency content of an AE signal and vertebral fracture has been reported[3,11,31]; however, in the current study there were no consistent trends observed when analysing the AE frequency characteristics for different fracture types (data not shown). Although these previous studies used the same AE sensor model as the current study, all AE sensors exhibit unique features in their frequency

response, and when not decoupled through sensor calibration, it is unknown how much the sensor-specific resonant response may affect the frequency characteristics of the AE signal. Whilst the absence of frequency-dependent characteristics in the current study may be linked to unidentified instrumentation issues, it is also likely to be related to the inhomogeneous nature of bony tissue, which would cause the AE signal to attenuate differently across the vertebral body, especially for higher frequencies within the trabecular bone.[22,30] To address this issue in future work, the use of more AE sensors to reduce the distance and, hence, AE signal attenuation between the fracture source and detector is recommended.

The maximum compressive forces corresponding to fracture presented in the current study compare favourably with those reported in previous experimental studies involving axial compression of three-vertebra lumbar specimens. For example, our measurements of maximum force corresponding to combined cortical and trabecular fractures (7.1 ± 1.9 kN; Table 2), was similar to the fracture load reported for burst fractures of T12 - L1-L2 (6.7 ± 2.0 kN),[28] and the compressive failure loads reported for various three-vertebra specimens (6-10 kN).[40] Previous measurements of yield force for axial compression of three-vertebra specimens (3.3 ± 1.2 kN and 4.2 ± 1.7 kN for rates of 10 mm/s and 2500 mm/s, respectively),[27] were observed to be lower than the equivalent measures in the current study (6.6 ± 1.5 kN). However, the specimens tested by Ochia et al.[27] were of low BMD (0.7 ± 0.1 g/cm^2), which may indicate that the bone was osteoporotic and have a lower fracture resistance. Whilst there are a number of previous studies where yield and ultimate strength characteristics for lumbar vertebrae have been reported,[14,34] this did not involve testing on three-vertebra lumbar spine specimens, a configuration which advantageously maintains the native boundary conditions of the centre vertebra.

There are a number of limitations of the present work. Twenty cadaveric spine specimens were used in the experimentation, which led to a small number of samples for each fracture type (n = 13 combined cortical and trabecular fractures and n = 5 isolated trabecular fractures). The total number of specimens tested was similar to that used in contemporary studies related to AE parameters of the human vertebrae.[11,36] Even with a greater number of specimens, it would be anticipated that an uneven distribution of fracture types would remain due to the practical challenge of producing isolated trabecular fractures under dynamic compression without causing further damage to the vertebral bone. Hence, it is recommended that the thresholds found in the current study for the AE and mechanical parameters be implemented in future work to enhance the rate of producing isolated trabecular fractures.

Another limitation of this study was that specimens were not imaged between each load increment. Consequently, the injury-free condition assumed for the initial 4% compressions of 14 specimens was not validated using imaging. However, the low compressive force of 2.1 ± 0.6 kN for these specimens was much lower than the range of yield and ultimate loads reported for lumbar vertebrae tested both as an isolated bone (9.0 ± 2.4)[34], as two-vertebra specimens with a lordotic posture (8.4±2.7 kN)[10], or within three-vertebra specimens (6.7 ± 2.0 kN).[28] A visual examination of each specimen indicated that there were no signs of bone fracture, and there was no change noted to measurements of the specimen stiffness. Based on these comparisons and observations, it was considered unlikely that the specimens had sustained any form of bone fracture for such low magnitude compression.

A final limitation was that only one AE sensor type was used in the mechanical testing. This restriction makes it difficult to establish whether the calibration of the AE

parameters improved the classification analysis, since both the calibrated and uncalibrated parameters may exhibit similar relative differences between tests. Such behaviour would likely explain the similar AUC observed between the uncalibrated AE_{energy} and most of the calibrated AE parameters (Tables 3 and 4). To clearly evaluate whether the calibration improved the fracture identification would require the application of the identified AE parameter thresholds on mechanical test using a different AE sensor, an application which is recommended in future work.

5 Conclusion

This study has demonstrated that AE parameters may be used to differentiate between vertebral body fractures of varying severity, with a classification performance that is comparable to mechanical parameters obtained from displacement and load cell readings. In particular, the AE parameters produced a slightly enhanced identification of isolated trabecular fractures which suggests that these sensors may better detect localised fracture that are less noticeable when considering the gross mechanical behaviour of a bone. The thresholds established for both the AE and mechanical parameters may be used to identify different fracture types with sensitivities over 100% and specificities of 80%, and it was demonstrated how these data may be extended to the analysis of the initiation of these fracture types. This study presents novel measurements of an AE signal that have been calibrated to provide measurements of AE wave pressure. This approach decouples the resonant response of the sensor from the AE signal, and allows the corresponding pressure measurements to be generalised to other calibrated AE sensors when examining vertebral fracture.

6 Acknowledgements

The authors would like to acknowledge the support from Defence Science and Technology Group, Australia and the collaboration with U.S. Army Research Laboratory for this research. We also acknowledge the facilities and scientific and technical assistance of the National Imaging Facility, a National Collaborative Research Infrastructure Strategy (NCRIS) capability, at Monash Biomedical Imaging, Monash University.

7 References

1. Agcaoglu, S., and O. Akkus. Acoustic Emission Based Monitoring of the Microdamage Evolution During Fatigue of Human Cortical Bone. *J. Biomech. Eng.* 135:081005, 2013.

2. Aggelis, D. G., M. Strantza, O. Louis, F. Boulpaep, D. Polyzos, and D. van Hemelrijck. Fracture of human femur tissue monitored by acoustic emission sensors. *Sensors* 15:5803–5819, 2015.

3. Arun, M. W. J., N. Yoganandan, B. D. Stemper, and F. A. Pintar. A methodology to condition distorted acoustic emission signals to identify fracture timing from human cadaver spine impact tests. *J. Mech. Behav. Biomed. Mater.* 40:156–160, 2014.

4. Burge, R., B. Dawson-Hughes, D. H. Solomon, J. B. Wong, A. King, and A. Tosteson. Incidence and economic burden of osteoporosis-related fractures in the United States, 2005-2025. *J. Bone Miner. Res.* 22:465–475, 2007.

5. Carretta, R., S. Lorenzetti, and R. Müller. Towards patient-specific material modeling of trabecular bone post-yield behavior. *Int. J. Numer. Meth. Bio.* 29:250–272, 2013.

6. Christen, P., S. Boutroy, R. Ellouz, R. Chapurlat, and B. Van Rietbergen. Least-detectable and age-related local in vivo bone remodelling assessed by time-lapse HR-pQCT. *PLoS One* 13:1–11, 2018.

7. Christiansen, B. A., and M. L. Bouxsein. Biomechanics of vertebral fractures and the vertebral fracture cascade. *Curr. Osteoporos. Rep.* 8:198–204, 2010.

8. Cormier, J., S. Manoogian, J. Bisplinghoff, C. McNally, and S. Duma. The use of acoustic emission in facial fracture detection. *Biomed. Sci. Instrum.* 44:147–152, 2008.

9. Crawford, R. P., C. E. Cann, and T. M. Keaveny. Finite element models predict in vitro vertebral body compressive strength better than quantitative computed tomography. *Bone* 33:744–750, 2003.

10. Curry, W. H., F. A. Pintar, N. B. Doan, H. S. Nguyen, G. Eckardt, J. L. Baisden, D. J.

Maiman, G. R. Paskoff, B. S. Shender, and B. D. Stemper. Lumbar spine endplate fractures: Biomechanical evaluation and clinical considerations through experimental induction of injury. *J. Orthop. Res.* 34:1084–1091, 2016.

11. Goodwin, B. D., F. A. Pintar, and N. Yoganandan. Acoustic Emission Signatures During Failure of Vertebra and Long Bone. *Ann. Biomed. Eng.* 45:1520–1533, 2017.

12. Griffin, J. Traceability of Acoustic Emission measurements for a proposed calibration method - Classification of characteristics and identification using signal analysis. *Mech. Syst. Signal Process.* 50–51:757–783, 2015.

13. Hagen, E. M., S. A. Lie, T. Rekand, N. E. Gilhus, and M. Gronning. Mortality after traumatic spinal cord injury: 50 years of follow-up. *J. Neurol. Neurosurg. Psychiatry* 81:368–373, 2010.

14. Hansson, T., B. Roos, and A. L. F. Nachemson. The bone mineral content and ultimate compressive strength of lumbar vertebrae. *Spine* 5:46–55, 1980.

15. Hasegawa, K., M. Abe, T. Washio, and T. Hara. An experimental study on the interface strength between titanium mesh cage and vertebra in reference to vertebral bone mineral density. *Spine* 26:957–963, 2001.

16. Hasserius, R., M. K. Karlsson, B. Jónsson, I. Redlund-Johnell, and O. Johnell. Long-term morbidity and mortality after a clinically diagnosed vertebral fracture in the elderly-a 12- and 22-year follow-up of 257 patients. *Calcif. Tissue Int.* 76:235–242, 2005.

17. Hurrell, A. Voltage to pressure conversion: are you getting `phased' by the problem? *J. Phys. Conf. Ser.* 1:57–62, 2004.

18. Jackman, T. M., A. I. Hussein, C. Curtiss, P. M. Fein, A. Camp, L. De Barros, and E. F. Morgan. Quantitative, 3D Visualization of the Initiation and Progression of Vertebral Fractures under Compression and Anterior Flexion. *J. Bone Miner. Res.* 31:777–788, 2016.

19. Juszczyk, M. M., L. Cristofolini, M. Salvà, L. Zani, E. Schileo, and M. Viceconti. Accurate in vitro identification of fracture onset in bones: Failure mechanism of the proximal human femur. *J. Biomech.* 46:158–164, 2013.

20. Landham, P. R., S. J. Gilbert, H. L. A. Baker-Rand, P. Pollintine, K. A. R. Brown, M. A. Adams, and P. Dolan. Pathogenesis of vertebral anterior wedge deformity : a 2-stage process? *Spine* 40:902–908, 2015.

21. Lane, N. E., M. C. Nevitt, H. K. Genant, and M. C. Hochberg. Reliability of new indices of radiographic osteoarthritis of the hand and hip and lumbar disc degeneration. *J. Rheumatol.* 20:1911–1918, 1993.

22. Lin, W., F. Serra-Hsu, J. Cheng, and Y.-X. Qin. Frequency specific ultrasound attenuation is sensitive to trabecular bone structure. *Ultrasound Med. Biol.* 38:2198–2207, 2012.

23. Liu, P. F., J. K. Chu, Y. L. Liu, and J. Y. Zheng. A study on the failure mechanisms of

carbon fiber/epoxy composite laminates using acoustic emission. *Mater. Des.* 37:228–235, 2012.

24. Martelli, S., and E. Perilli. Time-elapsed synchrotron-light microstructural imaging of femoral neck fracture. *J. Mech. Behav. Biomed. Mater.* 84:265–272, 2018.

25. Mattes, D., D. R. Haynor, H. Vesselle, T. K. Lewellen, and W. Eubank. PET-CT image registration in the chest using free-form deformations. *IEEE Trans. Med. Imaging* 22:120–128, 2003.

26. Morgan, E. F., H. H. Bayraktar, and T. M. Keaveny. Trabecular bone modulus-density relationships depend on anatomic site. *J. Biomech.* 36:897–904, 2003.

27. Ochia, R. S., and R. P. Ching. Internal pressure measurements during burst fracture formation in human lumbar vertebrae. *Spine* 27:1160–1167, 2002.

28. Panjabi, M. M., T. R. Oxland, M. Kifune, M. Arand, L. Wen, and A. Chen. Validity of the three-column theory of thoracolumbar fractures. A biomechanic investigation. *Spine* 20:1122–1127, 1995.

29. Pickett, G. E., M. Campos-Benitez, J. L. Keller, and N. Duggal. Epidemiology of traumatic spinal cord injury in Canada. *Spine* 31:799–805, 2006.

30. Sasso, M., G. Haïat, Y. Yamato, S. Naili, and M. Matsukawa. Frequency Dependence of Ultrasonic Attenuation in Bovine Cortical Bone: An In Vitro Study. *Ultrasound Med. Biol.* 33:1933–1942, 2007.

31. Shridharani, J. K., B. R. Bigler, C. A. Cox, M. A. Ortiz-Paparoni, and C. R. Bass. Sensitive Injury Detection in the Cervical Spine Using Acoustic Emission and Continuous Wavelet Transform. In: IRCOBI Conference 2016, Malaga, Spain, pp. 131-142, 2016. http://www.ircobi.org/wordpress/downloads/irc16/pdf-files/24.pdf

32. Stemper, B. D., S. Chirvi, N. Doan, J. L. Baisden, D. J. Maiman, W. H. Curry, N. Yoganandan, F. A. Pintar, G. Paskoff, and B. S. Shender. Biomechanical tolerance of whole lumbar spines in straightened posture subjected to axial acceleration. *J. Orthop. Res.* 1–10, 2017.

33. Stemper, B. D., S. G. Storvik, N. Yoganandan, J. L. Baisden, R. J. Fijalkowski, F. A. Pintar, B. S. Shender, and G. R. Paskoff. A new PMHS model for lumbar spine injuries during vertical acceleration. *J. Biomech. Eng.* 133:081002, 2011.

34. Stemper, B. D., N. Yoganandan, J. L. Baisden, S. Umale, A. S. Shah, B. S. Shender, and G. R. Paskoff. Rate-dependent fracture characteristics of lumbar vertebral bodies. *J. Mech. Behav. Biomed. Mater.* 41:271–279, 2015.

35. Taddei, F., L. Cristofolini, S. Martelli, H. S. Gill, and M. Viceconti. Subject-specific finite element models of long bones: An in vitro evaluation of the overall accuracy. *J. Biomech.* 39:2457–2467, 2006.

36. Van Toen, C., J. Street, T. R. Oxland, and P. A. Cripton. Acoustic emission signals can discriminate between compressive bone fractures and tensile ligament injuries in the

spine during dynamic loading. *J. Biomech.* 45:1643–1649, 2012.

37. Vasquez, K. B., F. T. Brozoski, K. P. Logsdon, and V. C. Chancey. Retrospective Analysis of Injuries in Underbody Blast Events: 2007-2010. *Mil. Med.* 183:347–352, 2018.

38. Wells, J. G., and R. D. Rawlings. Acoustic emission and mechanical properties of trabecular bone. *Biomaterials* 6:218–224, 1985.

39. Wenzel, T. E., M. B. Schaffler, and D. P. Fyhrie. In vivo trabecular microcracks in human vertebral bone. *Bone* 19:89–95, 1996.

40. Willén, J., S. Lindahl, L. Irstam, B. Aldman, and A. Nordwall. The thoracolumbar crush fracture an experimental study on instant axial dynamic loading: The resulting fracture type and its stability. Spine 9:624–631, 1984.

41. Yeh, O. C., and T. M. Keaveny. Relative roles of microdamage and microfracture in the mechanical behavior of trabecular bone. *J. Orthop. Res.* 19:1001–1007, 2001.

42. Yoganandan, N., J. Moore, F. A. Pintar, A. Banerjee, N. DeVogel, and J. Zhang. Role of disc area and trabecular bone density on lumbar spinal column fracture risk curves under vertical impact. *J. Biomech.* 72:90–98, 2018.

43. Yoganandan, N., F. A. Pintar, B. D. Stemper, J. L. Baisden, R. Aktay, B. S. Shender, G. Paskoff, and P. Laud. Trabecular bone density of male human cervical and lumbar vertebrae. *Bone* 39:336–344, 2006.

44. Zhao, F. D., P. Pollintine, B. D. Hole, M. A. Adams, and P. Dolan. Vertebral fractures usually affect the cranial endplate because it is thinner and supported by less-dense trabecular bone. *Bone* 44:372–379, 2009.

8 Tables

Table 1: Descriptive characteristics for the subjects corresponding to the three-vertebra specimens used in the mechanical testing

Combination	Number of specimens	Age (yrs)	Body height (cm)	Body weight (kg)	BMI (kg/m^2)	vBMD (mg/cm^3)
T12-L1-L2	2	62.5±2.1	183.0±0.0	91.0±9.9	27.2±3.0	136.3±43.2
L1-L2-L3	4	61.0±12.5	180.0±17.9	84.8±25.6	25.5±3.1	154.5±24.2
L2-L3-L4	5	65.6±10.7	171.4±3.4	83.3±24.0	27.9±13.7	166.3±72.8
L3-L4-L5	5	57.4±7.8	177.6±6.4	80.9±37.4	23.5±6.0	171.6±56.1
L4-L5-S1	4	60.3±12.1	186.3±10.4	74.4±20.1	26.3±2.2	165.5±71.5
Total	20	61.3±9.7	178.8±10.4	83.3±24.0	25.9±7.2	162.1±53.7

BMI, Body mass index; vBMD, volumetric bone mineral density of vertebral body trabecular bone

Table 2: Descriptive characteristics, AE and mechanical parameters observed for each injury category. Significant differences in variables between the different categories is indicated by the p-value[a]

		Injury category			p-value		
	Variable	Category 1: No fracture n=22	Category 2: Isolated trabecular fracture n=5	Category 3: Combined trabecular and cortical fracture n=13	Category 1 vs Category 2	Category 1 vs Category 3	Category 2 vs Category 3
Descriptive characteristics	No. of tests per specimen	1.0±0.0	3.8±1.5	3.2±1.6	N/A	N/A	0.598
	h_{VB+IVD} (mm)	38.8±1.7	35.2±3.7	39.2±1.7	0.022	0.978	0.012
	h_{mid} (mm)	51.5±3.8	45.2±6.0	51.5±3.2	0.085	0.092	0.054
	a_{VB} (mm^2)	1459.0±156.8	1436.9±172.4	1413.6±114.2	0.892	0.225	0.758
	EA (kN)	4862.5±1952.2	5116.2±1953.9	3608.3±858.5	0.913	0.095	0.122
	vBMD (mg/cm^3)	213.1±99.0	230.4±134.0	153.7±36.3	0.070	0.275	0.707
	Intervertebral disc grading	1.0±0.7	1.0±1.0	0.9±0.9	1.000	1.000	1.000
AE parameters	AE_{energy} (10^{-3} V^2s)	0.1±0.4	23.5±45.7	367.2±438.8	0.002	<0.001	0.076
	$AE_{exposure}$ (10^3 $Pa^2 \cdot s$)	8.4±23.1	3108.4±6337.7	40165.7±55081.0	0.002	<0.001	0.246
	$AE_{amplitude}$ (Pa)	213.6±331.1	4051.0±6448.4	17858.5±16812.2	0.002	<0.001	0.246
	AE_{counts} (n)	9.9±13.4	277.4±348.4	265.3±272.2	0.029	<0.001	0.988
	$AE_{risetime}$ (ms)	0.1±0.1	1.3±1.0	4.1±7.2	<0.001	<0.001	0.956
	$AE_{duration}$ (ms)	0.2±0.2	4.8±4.3	6.0±4.1	0.003	<0.001	0.445

Mechanical parameters	Specimens with Yield State = 1.0 (n)	4	5	13			
	$F_{z,Y}$ (N)	7005.6±2011.8	7495.9±2848.7	6626.8±1536.8	0.847	0.178	0.494
	$\sigma_{z,Y}$ (MPa)	4.3±1.2	5.2±1.7	4.8±1.2	0.367	0.178	0.956
	$F_{z,max}$ (N)	3412.1±2709.0	8301.1±3104.3	7083.7±1850.0	0.006	<0.001	0.494
	$\sigma_{z,max}$ (MPa)	2.3±1.6	5.7±1.9	5.1±1.6	0.003	<0.001	0.854
	$\varepsilon_{z,max}$ (%)	0.06±0.04	0.17±0.05	0.20±0.06	0.003	<0.001	0.598
	$\Delta F_{z,max}$ (N)	39.4±148.4	590.6±441.5	2603.0±1892.2	0.008	<0.001	0.012
	$\Delta\sigma_{z,max}$ (MPa)	0.0±0.1	0.4±0.3	1.9±1.4	0.008	<0.001	0.012

$h_{VB+IVD,}$ anterior height of the centre vertebral body and lower intervertebral disc; h_{mid}, mid-body height of the centre vertebral body and intervertebral discs; a_{VB}, cross-sectional area at the axial mid-plane of centre vertebral body; EA, axial rigidity; vBMD, volumetric bone mineral density of vertebral body trabecular bone; AE_{energy}, $AE_{exposure}$, $AE_{amplitude}$, AE_{counts}, $AE_{risetime}$ and $AE_{duration}$, acoustic emission energy, exposure, amplitude, counts, rise time and duration, respectively; $F_{z,Y}$ and $\sigma_{z,Y}$, yield force and stress, respectively; $F_{z,max}$, $\sigma_{z,max}$ and $\varepsilon_{z,max}$, maximum force, stress and strain, respectively; $\Delta F_{z,max}$ and $\Delta\sigma_{z,max}$, drop in compressive force and stress, respectively, following the peak force.

[a]All data pertaining to AE parameters was obtained for the AE sensor with the greater $AE_{amplitude}$.

Table 3: Sensitivity, specificity, accuracy and area under curve (AUC) of receiver operative characteristic curve for classification between Category 1 (no fracture) and Category 2 (Isolated trabecular fracture) and corresponding discrimination threshold[a,b]

	Variable	Sensitivity (%)	Specificity (%)	Accuracy (%)	Accuracy, second AE sensor (%)	AUC (95% CI)	Threshold
AE parameters	AE_{energy}	100.0	81.8	85.2	91.6	0.95 (0.87-1.00)***	0.05e-3 $V^2 \cdot s$
	$AE_{exposure}$	100.0	86.4	88.9	94.0	0.97 (0.91-1.00)***	5713.9 $Pa^2 \cdot s$ (71.5 dB re 400 $\mu Pa^2 \cdot s$)
	$AE_{amplitude}$	100.0	86.4	88.9	87.3	0.95 (0.88-1.00)***	461.9 Pa (173.3 dB re 1 µPa)
	AE_{counts}	80.0	86.4	85.2	92.1	0.85 (0.60-1.00)**	21
	$AE_{risetime}$	100.0	90.9	92.6	94.7	0.97 (0.92-1.00)***	0.31 ms
	$AE_{duration}$	100.0	95.5	96.3	96.3	0.98 (0.94-1.00)***	0.63 ms
Mechanical parameters	Yield State	100.0	81.8	85.2	N/A	0.91 (0.83-0.99)***	1.0
	$F_{z,max}$	100.0	77.3	81.5	N/A	0.90 (0.78-1.00)***	3810.9 N
	$\sigma_{z,max}$	100.0	81.8	85.2	N/A	0.93 (0.81-1.00)***	3.3 MPa
	$\varepsilon_{z,max}$	100.0	81.8	85.2	N/A	0.95 (0.86-1.00)***	0.09%
	$\Delta F_{z,max}$	80.0	95.5	92.6	N/A	0.87 (0.66-1.00)***	282.1 N
	$\Delta\sigma_{z,max}$	80.0	95.5	92.6	N/A	0.87 (0.66-1.00)***	0.18 MPa

AE_{energy}, $AE_{exposure}$, $AE_{amplitude}$, AE_{counts}, $AE_{risetime}$ and $AE_{duration}$, acoustic emission energy, exposure, amplitude, counts, rise time and duration, respectively; $F_{z,Y}$ and $\sigma_{z,Y}$, yield force and stress, respectively; $F_{z,max}$, $\sigma_{z,max}$ and $\varepsilon_{z,max}$, maximum force, stress and strain, respectively; $\Delta F_{z,max}$ and $\Delta\sigma_{z,max}$, drop in compressive force and stress, respectively, following the peak force.

[a]Significance of AUC tested with respect to null hypothesis (i.e., classification based on chance).

[b]Unless specified, all data pertaining to AE parameters was obtained for the AE sensor with the greater $AE_{amplitude}$.

** p<0.01; *** p<0.001

Table 4: Sensitivity, specificity, accuracy and area under curve (AUC) of receiver operative characteristic curve for classification between Category 1: No fracture and Category 3: Combined cortical and trabecular fracture and corresponding discrimination threshold[a,b]

	Variable	Sensitivity (%)	Specificity (%)	Accuracy (%)	Accuracy, second AE sensor (%)	AUC (95% CI)	Threshold
AE parameters	AE_{energy}	100.0	84.6	90.3	88.4	0.98 (0.94-1.00)***	2.77e-3 $V^2 \cdot s$
	$AE_{exposure}$	100.0	86.4	91.5	89.2	0.98 (0.95-1.00)***	3945.1 $Pa^2 \cdot s$ (69.9 dB re 400 $\mu Pa^2 \cdot s$)
	$AE_{amplitude}$	92.3	95.5	94.3	89.3	0.98 (0.93-1.00)***	642.7 Pa (176.2 dB re 1 µPa)
	AE_{counts}	76.9	100.0	91.4	79.7	0.92 (0.82-1.00)***	81.5
	$AE_{risetime}$	84.6	100.0	94.3	81.0	0.97 (0.93-1.00)***	0.65 ms
	$AE_{duration}$	92.3	95.5	94.3	87.9	0.98 (0.95-1.00)***	0.66 ms
Mechanical parameters	Yield State	100.0	81.8	88.6	N/A	0.91 (0.82-1.00)***	1.0
	$F_{z,max}$	100.0	77.3	85.7	N/A	0.87 (0.75-1.00)***	4080.0 N
	$\sigma_{z,max}$	92.3	86.4	88.6	N/A	0.90 (0.80-1.00)***	3.6 MPa
	$\varepsilon_{z,max}$	100.0	90.9	94.3	N/A	0.99 (0.96-1.00)***	0.12%
	$\Delta F_{z,max}$	100.0	100.0	100.0	N/A	1.00 (1.00-1.00)***	711.4 N
	$\Delta\sigma_{z,max}$	100.0	100.0	100.0	N/A	1.00 (1.00-1.00)***	0.5 MPa

AE_{energy}, $AE_{exposure}$, $AE_{amplitude}$, AE_{counts}, $AE_{risetime}$ and $AE_{duration}$, acoustic emission energy, exposure, amplitude, counts, rise time and duration, respectively; $F_{z,Y}$ and $\sigma_{z,Y}$, yield force and stress, respectively; $F_{z,max}$, $\sigma_{z,max}$ and $\varepsilon_{z,max}$, maximum force, stress and strain, respectively; $\Delta F_{z,max}$ and $\Delta\sigma_{z,max}$, drop in compressive force and stress, respectively, following the peak force.

[a]Significance of AUC tested with respect to null hypothesis (i.e., classification based on chance).

[b] Unless specified, all data pertaining to AE parameters was obtained for the AE sensor with the greater $AE_{amplitude}$.

*** $p<0.001$

9 Figure captions

Fig. 1. Specimen-specific measurements obtained from CT images. (**a)** Sagittal view depicting the mid-plane of the centre vertebral body (dashed white line). h_{VB+IVD}, was the distance in the z-direction between the anterior aspect of the cranial endplates of the centre and inferior vertebrae, and h_{mid} was the z-direction distance from the centroid of the cranial endplate of the upper disc to the centroid of the caudal endplate of the lower disc. The x- and z-axes point to the anterior and inferior directions, respectively, with the z-axis defined to be perpendicular to the vertebral body mid-plane. (**b)** Axial view of mid-plane of the centre vertebral body. The yellow and black circle represents the modulus-weighted centroid of the vertebral body and the grid shows the CT image voxels (enlarged for visualisation here). The x- and y-axes point to the right and anterior directions, respectively. E_i, and a_i are, respectively, the Young's modulus and area of voxel i.

Fig. 2: Schematic of the instrumentation and mechanical test configuration. (**a)** Sagittal view of the three-vertebra specimen. The position of the potting material and the left AE sensor are indicated. (**b)** Frontal view of the centre vertebra depicting the position of the left and right AE sensors.

Fig. 3: Calculation of the AE wave pressure. (**a)** Manufacturer-supplied sensitivity curve for an AE sensor used in the current study. **(b)** Measured AE voltage. (**c)** Fast-Fourier transform (FFT) amplitude of the AE voltage. (**d)** AE wave pressure calculated by dividing the AE voltage FFT by the sensitivity curve, then converting the signal back to the time domain via its inverse Fast-Fourier transform.

Fig. 4: Schematic of the AE parameters used in this study. AE bursts representing discrete periods of AE activity (shaded rectangles) and the threshold to eliminate background noise (10 Pa; dashed line) are indicated. Parameters were as follows: $AE_{amplitude}$, absolute maximum of the AE signal; AE_{counts}, number of times the AE signal crosses the threshold for background noise; $AE_{risetime}$, time from start to the signal peak of the AE burst containing $AE_{amplitude}$; $AE_{duration}$, interval of AE burst containing $AE_{amplitude}$. Note the sign of the AE signal was adjusted to ensure $AE_{amplitude}$ corresponded to a positive pressure.

Fig. 5: Schematic of the mechanical parameters used in this study. Parameters were as follows: $\sigma_{z,Y}$, yield stress; $\sigma_{z,max}$, maximum stress; $\Delta\sigma_z$, drop in stress following peak stress. The yield point was identified by offsetting the slope of the linear portion of the curve by a +0.2% strain. For this representative compression test, the presence of yielding was designated with a Yield State of 1.0.

Fig. 6: Identification of an isolated trabecular fracture for a representative specimen. (**a)** Pre-test image showing the boundary of the 1 mm cube. (**b)** Post-test image indicating the boundary of the 1 mm cube. (**c)** Boolean subtraction of a pre- and post-test DICOM image with an identified region with possible fractured bone. (**d)** 3D geometry of segmented pre-test bone. (**e)** 3D geometry of segmented post-test bone. The region of bone from the pre-test image that was dislodged during testing is shown in red. (**f)** Close-up view of the identified region. The high pixel intensity indicates a large difference between the pre- and post-test images.

Fig. 7: Dominant fracture types observed for Category 3: Combined cortical and trabecular fracture. **(a)** Pre- and post-test surface geometry of a representative vertebra that sustained a cranial endplate fracture (arrow). **(b)** Pre- and post-test surface geometry of a representative vertebra that sustained a split coronal fracture, as indicated by arrows.

Fig. 8: Representative measurements of displacement, force and AE signal for repeated tests on a representative specimen of each fracture type. The yield point and $AE_{amplitude}$ thresholds that distinguish the different fracture statuses are indicated. **(a) – (c)** Displacement, force and AE signal for Category 2: Isolated trabecular fracture. **(d) – (e)** Displacement, force and AE signal for Category 3: Combined cortical and trabecular fracture. Note: The AE signal corresponds to the sensor with the largest AE amplitude.

Fig. 1

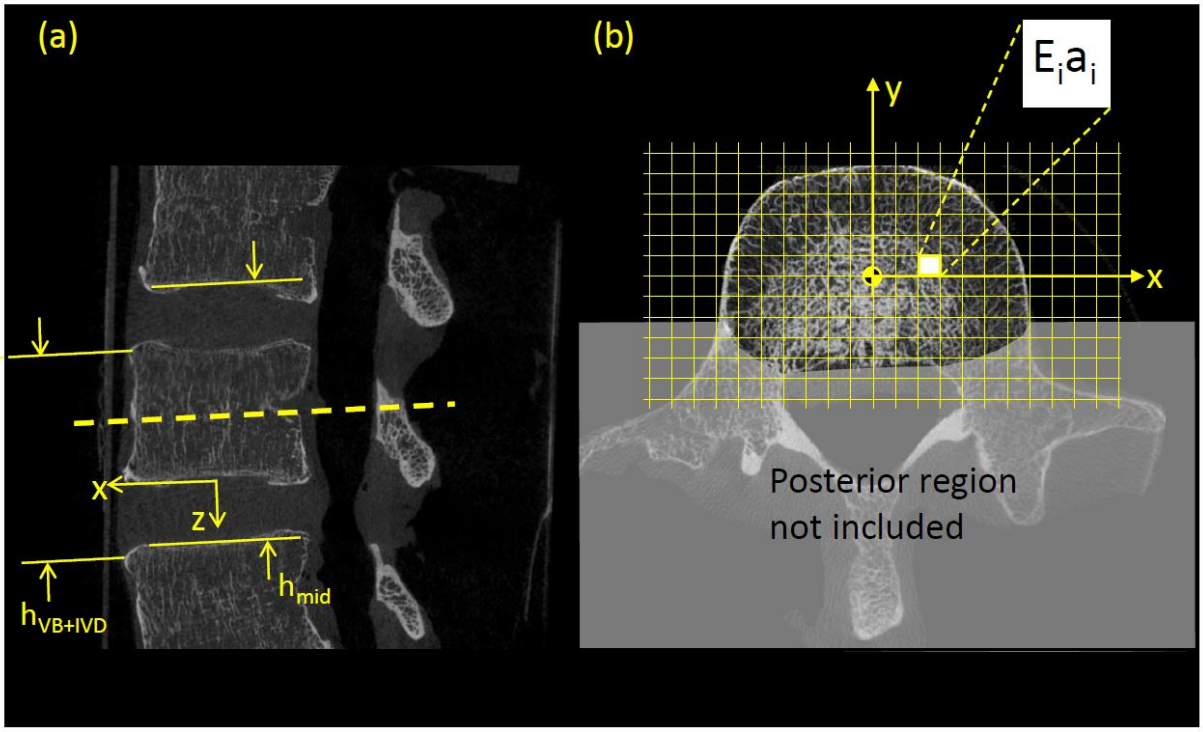

Fig. 2

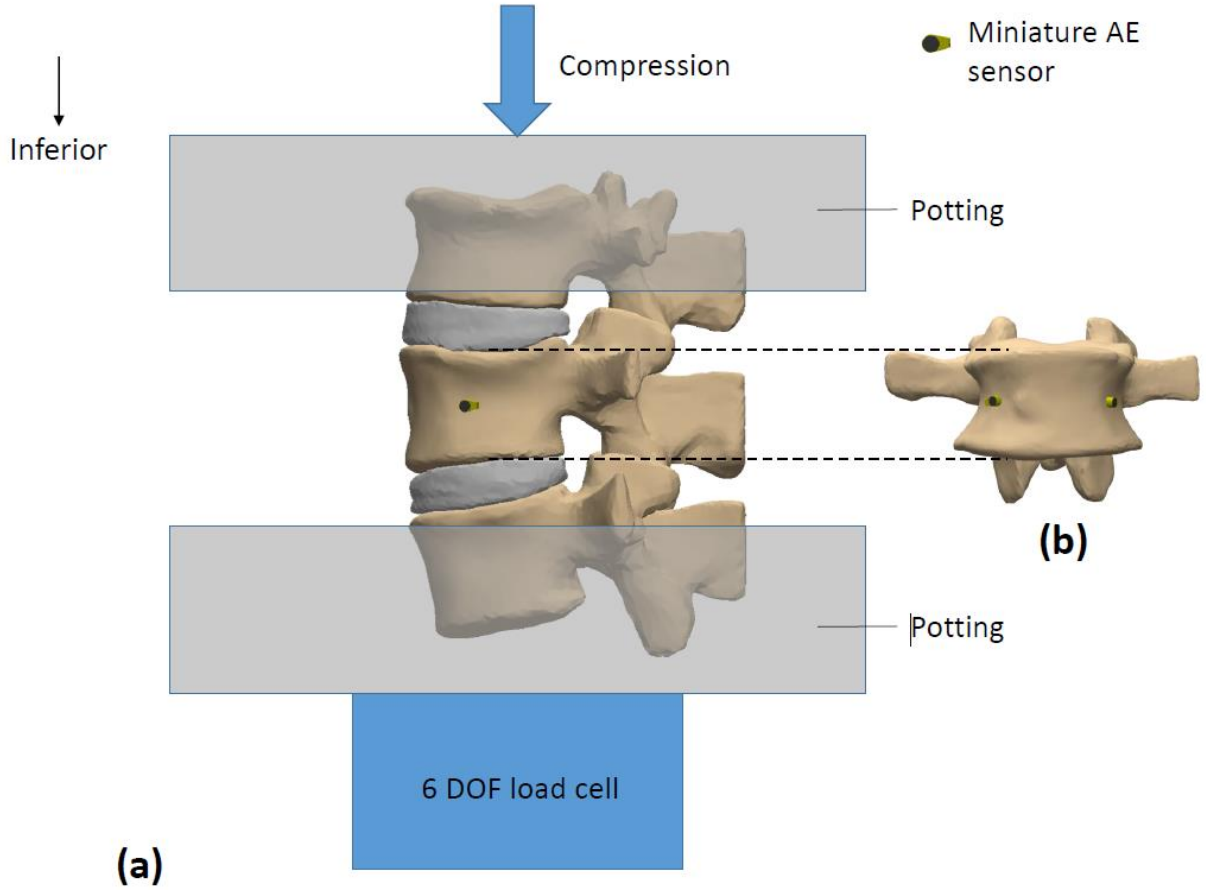
Compression
Miniature AE sensor
Inferior
Potting
(b)
Potting
6 DOF load cell
(a)

Fig. 3

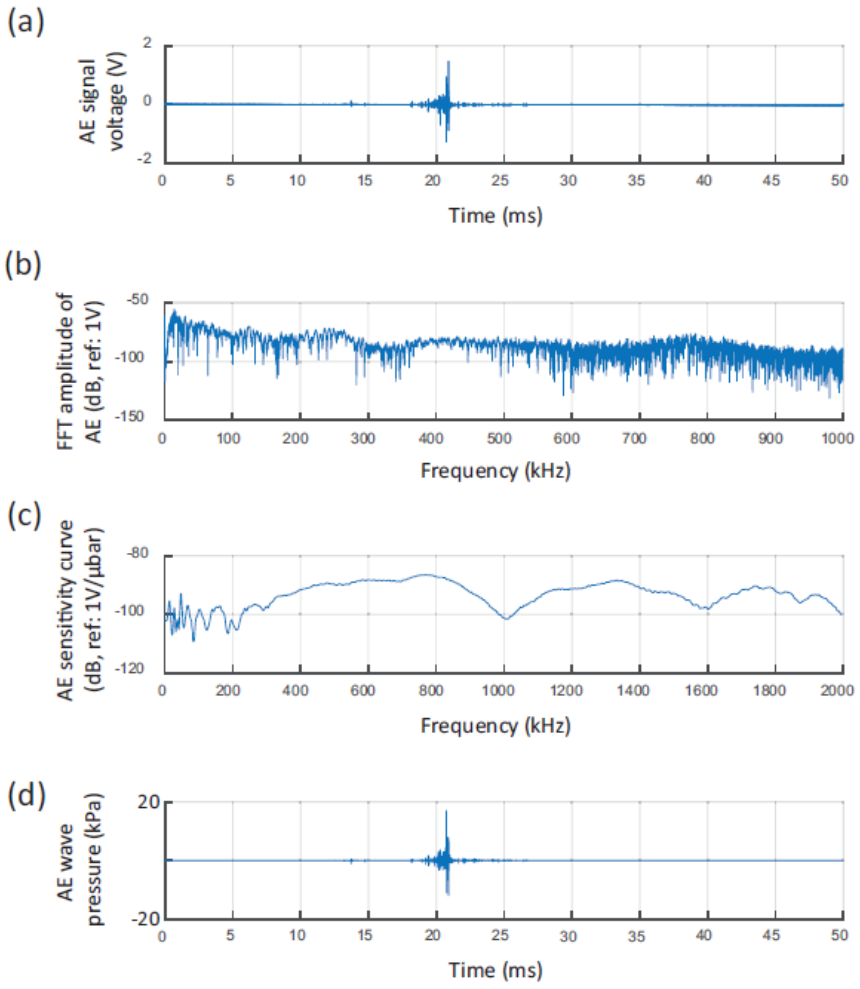
(a)
AE signal voltage (V)
2
0
-2
0 5 10 15 20 25 30 35 40 45 50
Time (ms)
(b)
FFT amplitude of AE (dB, ref: 1V)
-50
-100
-150
0 100 200 300 400 500 600 700 800 900 1000
Frequency (kHz)
(c)
AE sensitivity curve (dB, ref: 1V/μbar)
-80
-100
-120
0 200 400 600 800 1000 1200 1400 1600 1800 2000
Frequency (kHz)
(d)
AE wave pressure (kPa)
20
-20
0 5 10 15 20 25 30 35 40 45 50
Time (ms)

Fig. 4

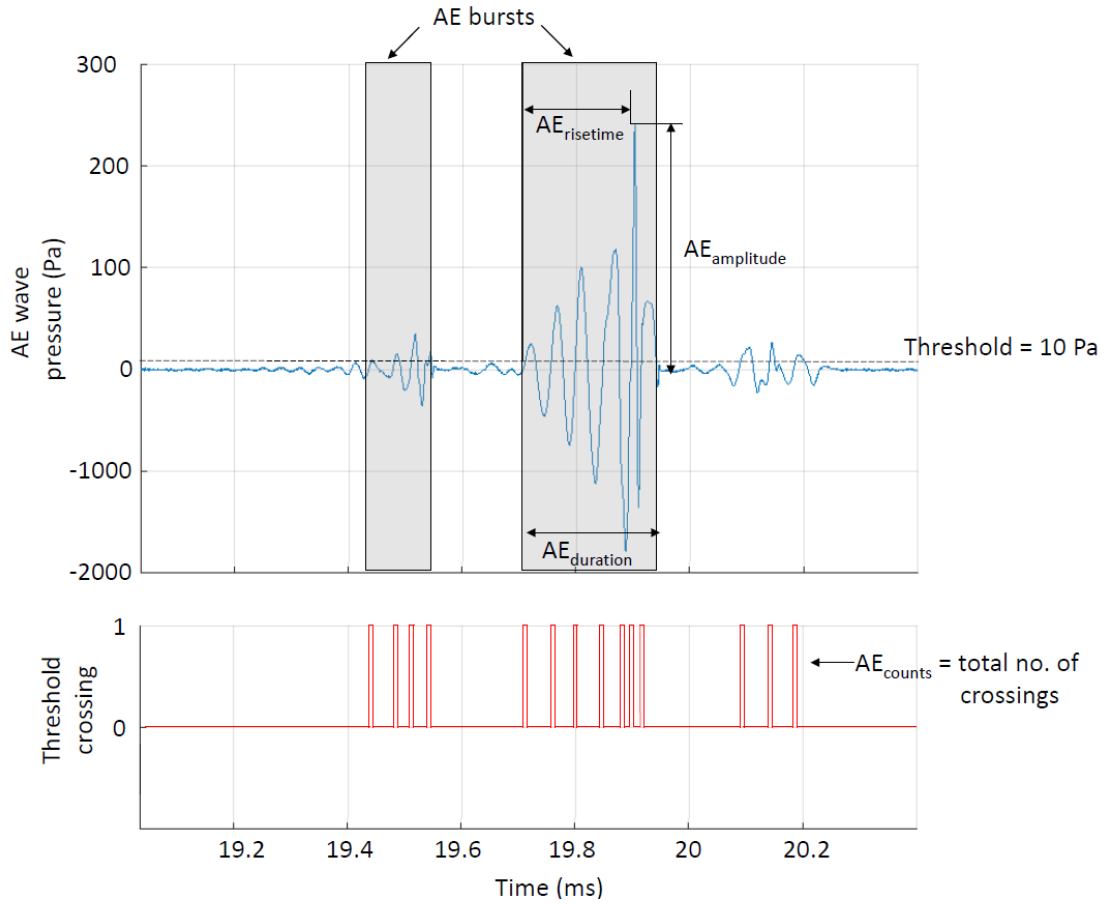
AE bursts
300
200
100
0
-1000
-2000
AE wave pressure (Pa)
AE$_{risetime}$
AE$_{amplitude}$
AE$_{duration}$
Threshold = 10 Pa
1
0
Threshold crossing
AE$_{counts}$ = total no. of crossings
19.2
19.4
19.6
19.8
20
20.2
Time (ms)

Fig. 5

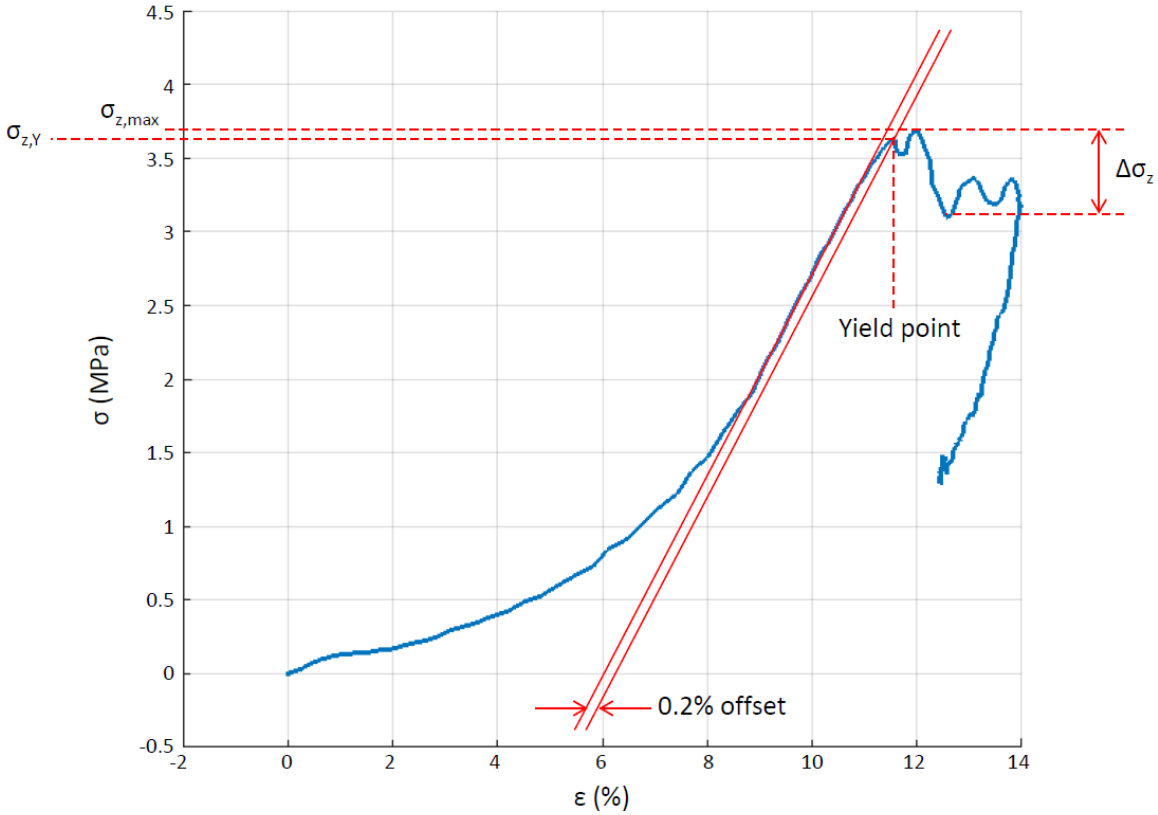
σz,max
σz,Y
Δσz
Yield point
0.2% offset
σ (MPa)
ε (%)
4.5
4
3.5
3
2.5
2
1.5
1
0.5
0
-0.5
-2
0
2
4
6
8
10
12
14

Fig. 6

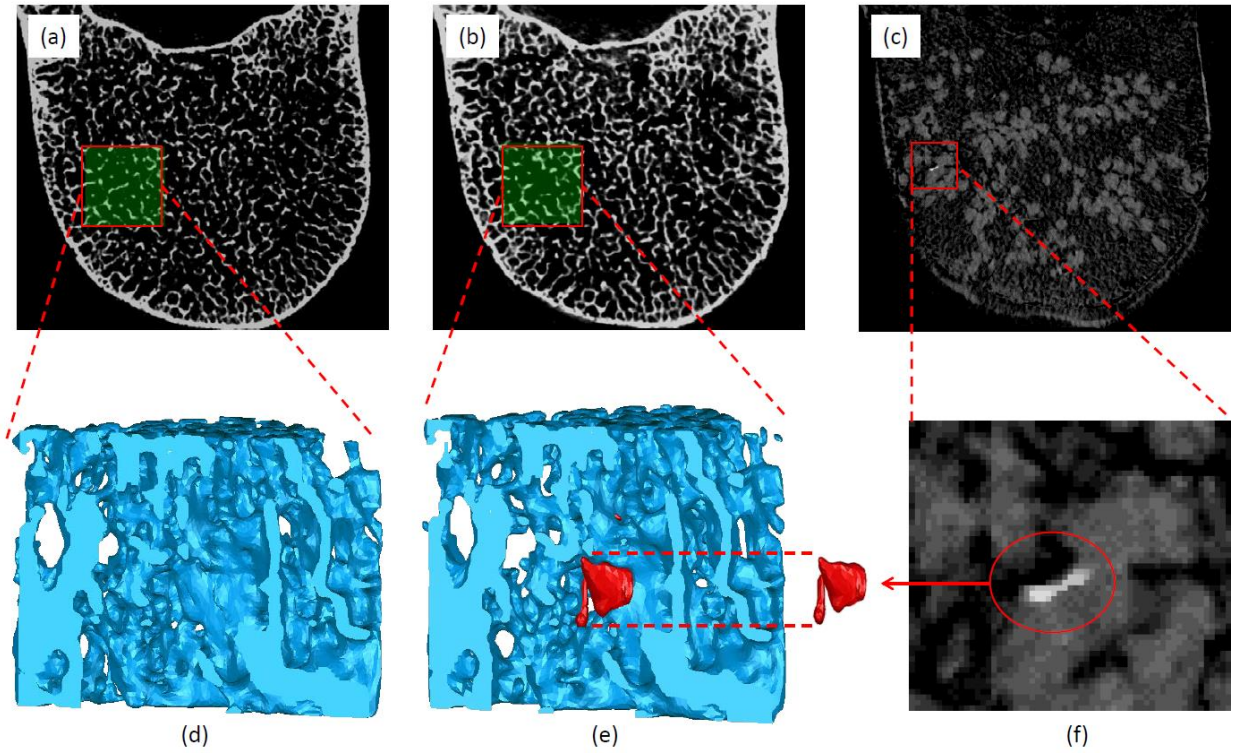

Fig. 7

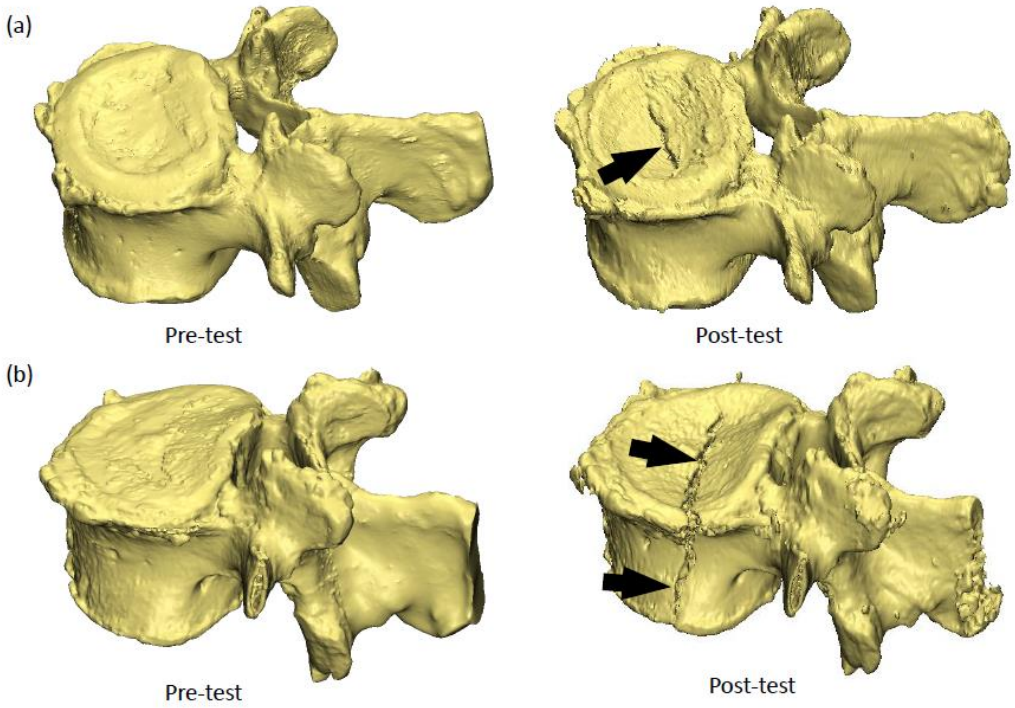

Fig. 8

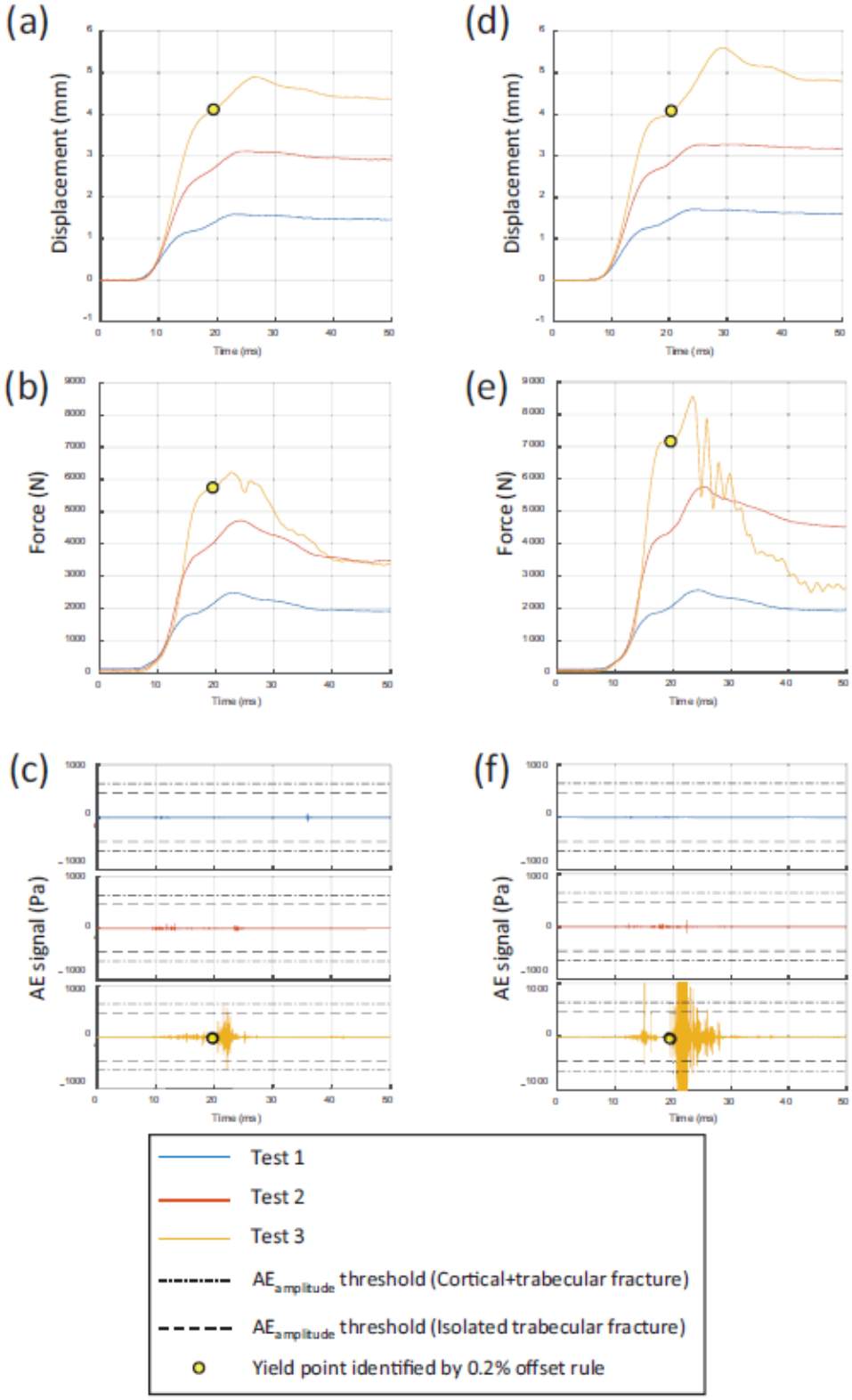
(a)
Displacement (mm)
Time (ms)
(d)
Displacement (mm)
Time (ms)
(b)
Force (N)
Time (ms)
(e)
Force (N)
Time (ms)
(c)
AE signal (Pa)
Time (ms)
(f)
AE signal (Pa)
Time (ms)
Test 1
Test 2
Test 3
AE amplitude threshold (Cortical+trabecular fracture)
AE amplitude threshold (Isolated trabecular fracture)
Yield point identified by 0.2% offset rule